Eur J Nucl Med Mol Imaging (2010) 37:1887–1902
DOI 10.1007/s00259-010-1488-z

ORIGINAL ARTICLE

A fast cardiac gamma camera with dynamic SPECT capabilities: design, system validation and future potential

Moshe Bocher · Ira M. Blevis · Leonid Tsukerman · Yigal Shrem · Gil Kovalski · Lana Volokh

Received: 31 October 2009 / Accepted: 27 April 2010 / Published online: 29 June 2010

Abstract
Purpose The goal of this study is to present the Discovery NM 530c (DNM), a cardiac SPECT camera, interfacing multi-pinhole collimators with solid-state modules, aiming at slashing acquisition time without jeopardizing quality. DNM resembles PET since it enables 3-D SPECT without detector motion. We further envision how these novel capabilities may help with current and future challenges of cardiac imaging.
Methods DNM sensitivity, spatial resolution (SR) and energy resolution (ER), count rate response, cardiac uniformity and cardiac defect contrast were measured and compared to a dedicated cardiac, dual-head standard SPECT (S-SPECT) camera.
Results DNM sensitivity was more than threefold higher while SR was notably better. Significantly, SR was the same for ^{99m}Tc and ^{201}Tl. ER was improved on DNM and allowed good separation of ^{99m}Tc and ^{123}I spectral peaks. Count rate remained linear on DNM up to 612 kcps, while S-SPECT showed severe dead time limitations. Phantom studies revealed comparable uniformity and defect contrast, notwithstanding significantly shorter acquisition time for the DNM. First patient images, including dynamic SPECT, are also presented.
Conclusion DNM is raising the bar for expedition and upgrade of practice. It features high sensitivity as well as improved SR, temporal resolution and ER. It enables reduction of acquisition time and fast protocols. Importantly, it is potentially capable of dynamic 3-D acquisition. The new technology is potentially upgradeable and may become a milestone in the evolution of nuclear cardiology as it assumes its key role in molecular imaging of the heart.

Keywords Cardiac gamma camera · Single photon emission computed tomography · Myocardial perfusion scintigraphy · Discovery NM 530c

M. Bocher (✉)
Hadassah Hospital, Hebrew University of Jerusalem,
Jerusalem, Israel
e-mail: moshe@hadassah.org.il

I. M. Blevis · L. Tsukerman · Y. Shrem · G. Kovalski · L. Volokh
Molecular Imaging, GE Healthcare,
Tirat Hacarmel, Israel

Introduction

The technique of SPECT for myocardial perfusion scintigraphy (MPS) is the most common, non-invasive imaging tool for risk stratification of patients with coronary artery disease (CAD) [1–5]. Millions of studies are performed each year, greatly exceeding other competing modalities [6], such as PET or MRI, in spite of some advantages offered by them. The growth of SPECT results from the vast extent of CAD worldwide and its associated morbidity and mortality, and enormous social and economic burden. This situation has created an urgent need for an efficient, non-invasive tool to risk-stratify patients and thus to direct and monitor therapy. The need has perpetuated a continuous effort to upgrade SPECT MPS [7–10].

Notwithstanding the growth and value of current standard SPECT (S-SPECT) practice, it is limited and needs to be transformed in order to remain a truly effective tool. Of foremost concern are the costs of the technique. Expenditures for health care in the USA have doubled over the last 10 years [11, 12] and cardiovascular disease accounts for 20% of these total costs. The growth rates of imaging costs continue to outpace other medical services

[13] and stress imaging has grown 6% per year from 1993 to 2001 [14]. While, in theory, cutting procedure time could have reduced costs, attempts to slash acquisition time are limited with current SPECT technology. This is due mainly to the low efficiency of the classic Anger gamma camera and its parallel-hole collimation, and additionally to the limited spatial resolution (SR) and energy resolution (ER) of the sodium iodide crystal and the process of light scintillation. Measurements of gamma photon position and energy are derived from the many signals produced by a large array of photomultiplier tubes. The individual signals are statistically poor, and this limits both the SR and ER. Limited ER leads to contamination of the image by scattered gamma photons, leading to further deterioration of SR and target to non-target contrast ratios. Marginal ER often leads to instability of uniformity corrections and degradation of the detector's uniformity of response. The collection of resulting errors may be propagated during attenuation-corrected SPECT reconstruction [15].

A more fundamental limitation of conventional MPS is the relative nature of its normalized output images. This occurs because the interpretation model relies, sometimes erroneously, on having at least one myocardial region with normal perfusion. In CAD that involves all three major arteries; the extent and severity of ischaemia will be reduced because of the image normalization, and often only the most severely underperfused areas will be detected [16–19]. Sometimes, in "balanced ischaemia" and in left main coronary stenosis, MPS may totally miss patients who have a very high-risk coronary disease. Since the extent of perfusion abnormality is critical in deciding which patients would benefit from coronary revascularization, such underestimation of the extent of disease is a major limitation of S-SPECT that needs to be overcome [20–22]. Several innovative attempts to measure myocardial blood flow (MBF) and coronary flow reserve (CFR) with S-SPECT technology have been carried out, but have not gained wide clinical acceptance [23–27]. This situation reflects both the recognition of the need for such measurements as well as the technical difficulties and limitations involved. Since MBF and CFR can be measured by PET [28, 29], a large body of respected researchers has been predicting the emergence of PET as the primary MPS tool for a considerable time [30–34]. Interestingly, such adoption of PET for MPS has not yet occurred despite the abundance of PET/CT scanners in recent years. The expressed customer preference may be related to the ease of use and availability of both SPECT radiopharmaceuticals and equipment.

Awareness of the above-mentioned limitations of S-SPECT motivated our team to design and create a new ultra-fast cardiac SPECT camera, denoted the Discovery NM 530c (DNM) (Fig. 1), in order to provide the medical community with the simultaneous benefits of both convenient and cost-effective logistics and improved image quality. The DNM technology combines a multi-pinhole collimator block interfaced with a multidetector array of pixelated cadmium zinc telluride (CZT) modules (Fig. 2). Its design is inspired by multi-pinhole collimation SPECT technology, introduced years ago [35], and by its recent adaptation for pre-clinical microSPECT as well as clinical SPECT [36–41].

In DNM, the detectors and pinholes are all focused on the heart organ in order to maximize the imaging sensitivity there. The miniature pixels and miniature size of the CZT modules allows the packing and arrangement of multiple detectors in DNM with sufficient proximity and coverage to ensure that 3-D sampling of the heart provided by stationary acquisition is sufficient for tomographic reconstruction. Unlike traditional pinhole collimation that uses magnification, in DNM imaging, minification is used (Fig. 2b). In this case system resolution is preserved because of the small pixels and high intrinsic resolution the CZT technology [40, 41]. This matching allows a reduction in detector size without loss of resolution. The savings in detector area allows the economical construction of multiple detectors, each with a full view of the heart. Since each detector is stationary, it has the full acquisition time to acquire the image. Even a few minutes of acquisition time is more than enough to outperform the sensitivity of a rotating S-SPECT camera, where typically

Fig. 1 *Left*: the Discovery NM 530c (DNM) featuring a gantry that is similar to a conventional cardiac SPECT camera, with a different detector assembly that is completely stationary during acquisition. *Right*: hybridization of the DNM camera with a multidetector CT camera

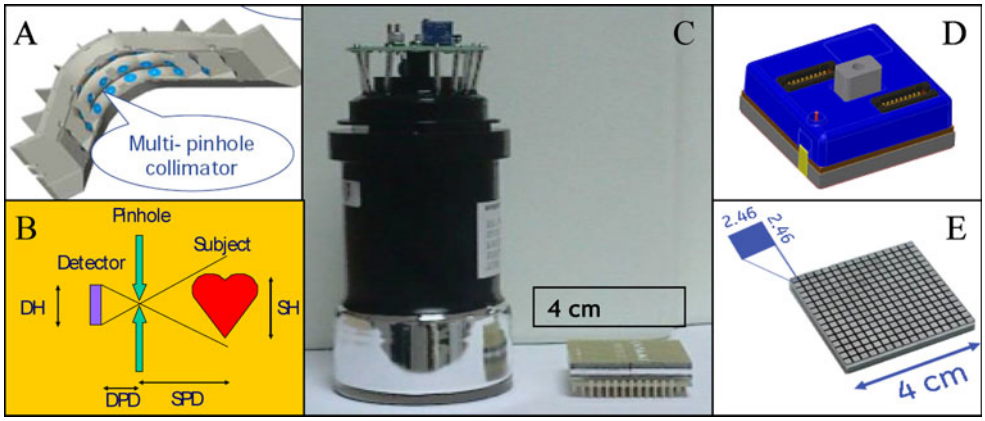

Fig. 2 Components of the detector assembly. **a** Multi-pinhole collimator covering the heart volume. **b** Pinhole collimation and miniaturization of the detector enable proximity to the heart with minification of the heart image, utilizing most of the detector surface to cover the heart projection. **c** A 4×4 cm CZT detector size as compared to a classic photomultiplier tube of a conventional SPECT camera. **d** The detector box with its rear electronic connections. **e** The CZT is pixelated featuring intrinsic resolution of about 2.5 mm irrespective of photon energy

only a few seconds are allocated to each projection. Thus, DNM is an inherently tomographic technology, which similar to PET is potentially capable of truly dynamic tomographic study that is required for quantitative MPS.

The aim of this manuscript is to describe the technological concepts underlying the DNM design, to measure and compare DNM features to state-of-the-art S-SPECT technology, and to forecast how those improved capabilities will promote new significant changes in clinical practice and may influence the evolution of nuclear cardiology.

Materials and methods

System description

The DNM gantry is similar to that of an S-SPECT gamma camera, yet its detector assembly is radically new. The detector assembly comprises a multi-pinhole collimator block, where each pinhole illuminates a solid-state pixelated, gamma ray detector made of CZT (Fig. 2). Thus, each pinhole and detector constitutes a complete miniature gamma camera.

In CZT, an absorbed gamma ray is converted directly to an electric charge. In S-SPECT with scintillation crystals, an absorbed gamma ray is first converted to ultraviolet light and only then to an electric charge in an "indirect" process. The indirect process is inefficient and is then followed by a high amplification step in the photomultiplier tube, resulting in limitation to the overall accuracy of the measured energy and position of the incident gamma rays. In CZT these limits are overcome by a "direct" signal of electron hole pairs that is ~50 times bigger than the signal being amplified in the S-SPECT system. Thus, the ER is dramatically improved by the statistics of the collected signal. A known limitation of the ER in CZT results from depth of interaction effects in the detector material; however, this effect is measurably reduced in pinhole collimation geometry because of the oblique angles of incidence which reduce both the mean depth of interaction and the variability of these depths [41].

The intrinsic SR of the CZT technology is determined by the combination of the pixel size where the gamma photons are absorbed and the system geometry. The CZT pixels are physically 2.46×2.46 mm in size and have negligible crosstalk due to the direct conversion to an electric charge. In contrast conventional S-SPECT pixels do share signals because of the spreading of light between them and this crosstalk degrades their effective pixel size. The optimized small pixel size of DNM allows a significant minification without loss of resolution compared to conventional systems. Overall, the DNM system detector contains 19 detector heads of 8×8 cm. The detector heads are directed towards the heart so as to sample signals from the heart and the region around it. The target volume for high quality imaging in which the patient heart is positioned is approximately a sphere of 19 cm diameter. Once the patient is positioned on the imaging table, the position of the gantry is adjusted so that the heart is close to the centre of the field of view (FOV). An automatic algorithm can guide the operator to the best positioning.

Importantly, the intrinsic SR is independent of photon energy. In particular, for isotopes with low energy photons like ^{201}Tl where intrinsic SR is a limiting factor for S-SPECT, the SR may be greatly improved and become similar to ^{99m}Tc. Another source for SR degradation in S-SPECT is septal penetration and scatter in the parallel-hole collimator by high energy photons emitted by ^{123}I and ^{201}Tl radiopharmaceuticals or from isotopic impurities. The well-shielded pinhole collimator may be free of these processes

and thus may provide equivalent resolution to that of the ^{99m}Tc. Each CZT pixel is an independent detector provided with its own electronic processing unit using miniaturized attached electronics (Fig. 2d). Therefore the DNM may be capable of linear detection response even at very high count rates. This is not possible with S-SPECT where only two independent detector electronic chains exist, one for each head of the camera, and therefore detector processing dead time results in significant event losses and pile-ups, at high count rates. Since the DNM gantry does not move during acquisition and since all detectors are acquiring data from the same source simultaneously, the measured projections are temporally consistent and the reconstructed data may be termed "inherent and instantaneously tomographic". In this respect DNM imaging resembles PET imaging that features temporal consistency of data acquired into projection views that may be beneficial for applications requiring dynamic information. The DNM is thus designed to acquire all types of cardiac SPECT procedures including multigated tomography and dynamic images. In addition to "on-the-fly" reconstruction the DNM saves each event of the acquired data in a list-mode format including its energy, spatial information, time of occurrence and gated ECG trigger, for later specialized analysis.

Reconstruction algorithm For DNM, dedicated image reconstruction was developed. SPECT reconstruction is based on an implementation of a 3-D iterative Bayesian reconstruction algorithm [42] combining accurate modelling of DNM geometrical and physical characteristics with optimized statistical techniques. An adaptation of one-step-late Green's prior [43] was used to control smoothness of the reconstruction; 30–50 iterations of the algorithm were used for reconstruction of phantom and clinical data. Post-reconstruction, a Butterworth filter with a cut-off frequency of 0.37 cycles/cm and power of 7 was applied. Fine-tuning of the reconstruction algorithm parameters, optimized separately per type of acquisition (e.g. low-dose, high-dose), was based on the optimal trade-off between reconstructed uniformity of healthy myocardium and contrast of perfusion defects, using extensive phantom studies [44].

In the following experiments, whenever it was relevant, we have compared imaging capabilities of the DNM system to a state-of-the-art, cardiac-dedicated, dual-head S-SPECT camera (Ventri, GE Healthcare).

SPECT sensitivity

The count sensitivity of the two cameras (DNM and S-SPECT) for ^{99m}Tc with energy window set at 140.5 keV ± 10% was compared using the cardiac insert of an anthropomorphic torso phantom (Data Spectrum), in air without any scatter material. The patient volume that is fully seen by all detectors is denoted the quality FOV (QFOV) For the DNM two different phantom locations were tested: (1) at the centre of the QFOV and (2) the point closest to the camera body within the QFOV. The same phantom was used for sequential sensitivity measurements on both DNM and S-SPECT systems. The measurements were corrected for decay. Sensitivity was calculated as counts/s per MBq.

Energy resolution

Spectra of ^{99m}Tc, ^{201}Tl and ^{123}I were measured using a method similar to the "intrinsic ER" test defined in NEMA NU-1 2001 standard section 2.2, on both DNM and S-SPECT detectors without collimation, using a point source. ER was calculated by measuring full-width at half-maximum (FWHM) as percentage of peak position. ER is important for scatter rejection from image data as well as intrinsic uniformity and calibration stability. In addition, energy spectra of combined ^{99m}Tc and ^{123}I were measured to evaluate simultaneous ^{99m}Tc/^{123}I dual isotope acquisition capabilities of both systems.

Collimator penetration in ^{123}I imaging

A ^{123}I point source of 88.8 MBq activity located at a distance of 15 cm from the collimator was imaged in planar mode on an S-SPECT system and in one of the DNM collimated detectors to visualize respective collimator penetration.

SPECT resolution (with scatter)

SPECT resolution with scatter was measured using three ^{99m}Tc point sources (1.5×1.5×1.5 mm) placed according to NEMA in a cylindrical phantom filled with water. The phantom centre was placed 15 cm away from the external surface of the collimator. The two-dimensional (X and Y) activity profiles were plotted and FWHM calculated for each of the three point sources; the results of the central, radial and tangential resolutions as defined by NEMA protocol are reported. The following reconstruction parameters were used for DNM: reconstruction type: maximum likelihood expectation maximization (MLEM), number of iterations: 250, reconstruction voxel size: 2×2×2 mm, and for S-SPECT: reconstruction type: filtered backprojection (FBP), reconstruction voxel size: 1.6×1.6×1.6 mm. No filters were used for both modalities. Additional similar measurements were performed for ^{201}Tl point sources. Note that while the S-SPECT result is fully compliant with NEMA protocols, FBP is not possible with the DNM and therefore the result is not compliant with the NEMA protocol.

Count rate performance

The count rate performances of the DNM and of the S-SPECT were measured to assess the count rate linearity, especially at high rates. Good count rate performance is crucial for quantitative dynamic SPECT applications, such as CFR measurements performed on data acquired during the passage of an injected bolus through the heart chambers. Since CFR and left ventricular ejection fraction (LVEF) measurements both require very high temporal resolution, of the order of 1 s or even faster, very high count rates are mandatory for a good image. However, high count rates often cause a non-linear camera response that significantly reduces accuracy. Therefore both high camera sensitivity and count rate linearity are required.

For S-SPECT, measurements were based on NEMA NU-1 guidelines and were performed accordingly: without collimation and using a decaying ^{99m}Tc source. Since multi-pinhole collimation is an integral part of the DNM system, the measurements were performed with collimation. The DNM measurements were performed using the multiple calibrated source method: 12 syringes with increasing activity from 199.8 to 1,994.3 MBq (53.9 mCi) of ^{99m}Tc were sequentially placed at the centre of the QFOV. The counts measurement was performed on S-SPECT using an acquisition mode that was dedicated for high count rates. The DNM has only one standard acquisition mode for all count rates. The energy window was the same for both systems, i.e. 140.5 keV ± 10%. The DNM was configured to stop the acquisition when the count rate exceeds a predetermined electronic throughput computer limit.

Phantom studies of ^{99m}Tc myocardial perfusion SPECT

Series of anthropomorphic torso phantom (Data Spectrum) acquisitions were performed in order to evaluate image quality in multiple imaging scenarios relevant to clinical practice. The main clinical task for MPS is detection and characterization of perfusion defects; thus useful images should achieve uniform uptake within normally perfused myocardium and delineate myocardial perfusion defects in pathological situations. To capture this, we have compared S-SPECT and DNM performance by measuring the trade-off between uniformity of normal myocardium and contrast of perfusion defects for manufacturer-recommended acquisition parameters with a standard camera and short acquisition times intended for clinical use of DNM.

Phantom preparation and acquisition

Image data were acquired using a Data Spectrum anthropomorphic torso phantom with heart, lungs and liver inserts, and with inserts simulating myocardial perfusion defects (Fig. 3). The phantom was prepared to simulate realistic ^{99m}Tc activities encountered during the low-dose rest and high-dose stress parts of the standard 1-day myocardial perfusion protocol. In addition, breast inserts were used to simulate variations of female anatomy and the liver inserts were loaded with normal and high activities. Perfusion defect inserts were placed in two different locations within the myocardial wall. Manufacturer-recommended parameters, including acquisition times, were used for the standard SPECT camera—12.5 min and 10 for low- (rest) and high-dose (stress) conditions, respectively. The standard acquisition protocol for the S-SPECT camera resulted in acquisition of 60 projections, evenly spaced over a 180° arc, from right anterior oblique to left posterior lateral view. DNM acquisition times were determined based on prior phantom experiments measuring ratios of volumetric sensitivity within the heart region, compared to S-SPECT, and were 5 and 3 min, respectively. Reconstruction parameters optimization for DNM was based on extensive prior phantom experimentation, aiming at optimal trade-offs between uniformity of healthy myocardium and reconstructed contrast of perfusion defect, which would be similar to those acceptable for traditional SPECT devices; 50 iterations of penalized maximum likelihood reconstruc-

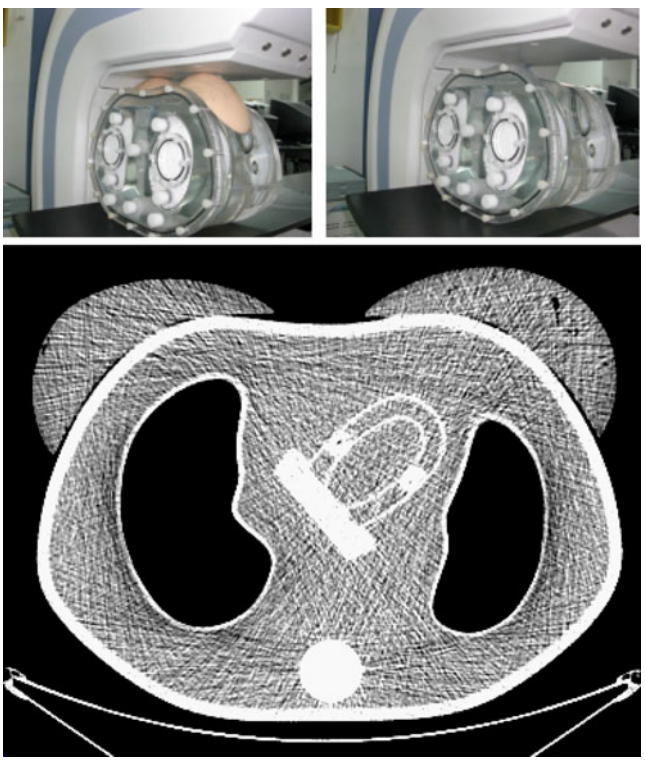

Fig. 3 Imaging of anthropomorphic torso phantom by the DNM camera with male (*upper right*) and female (*upper left*) configurations. *Bottom*: transaxial CT slice of the phantom with middle-sized breast extensions and defect inserts in septal and lateral walls

tion were used for high-dose acquisitions and 40 iterations for low-dose acquisitions. Post-reconstruction, a 3-D Butterworth filter was applied with the following parameters: cut-off frequency of 0.37 cycles/cm and power of 7.

Uniformity-contrast analysis

For the purpose of uniformity-contrast analysis, registered phantoms of uniform activity and those containing defect pairs were acquired in series containing five to ten repetitions for each condition. Reconstructed transaxial slices were re-oriented into standard cardiac oblique images. Stacks of short-axes slices were used for myocardial wall segmentation and measurement of reconstructed activity at the left ventricular wall surface using standard myocardial perfusion segmentation software (LVSD, GE Healthcare). These values were used for calculation of uniformity and contrast metrics. Normalized standard deviation (NSD) was used to characterize uniformity for healthy heart with uniform activity and effective contrast (EC) to characterize reconstructed contrast for known defect locations and volumes. The metrics were calculated as follows:

$$NSD = \frac{SD(c)}{c} \bullet 100\%$$

$$EC = \frac{\overline{c}^{(-)}_{i\in D} - \overline{c}^{(+)}_{i\in D}}{\overline{c}^{(-)}_{i\in D}} \bullet 100\%$$

where $\overline{c}^{(+)}_{i\in D}$ is the mean estimated count on mid-myocardial surface in the known volume of defect insert in defect-present (+) phantom, while (-) denotes an area without a defect. NSD/EC plots were generated for matching sets of DNM and S-SPECT data. We further compared DNM reconstructed perfusion distribution with S-SPECT for a series of uniform phantoms. Data consistency was analysed using normalized activity scores in myocardial segments conforming to a 17-segment heart model [45]. A segmental score S was defined as the ratio of mean value on the mid-myocardial surface within the segment to maximum value on the mid-myocardial surface across the entire myocardium. Correlation for segmental scores between DNM and S-SPECT over a number of phantom measurements was performed.

Dynamic SPECT

A total of 370 MBq of ^{99m}Tc-MIBI was injected in a resting patient's left arm while lying on the camera table. A list-mode dynamic acquisition was started simultaneously with the injection and continued for 5 min, allowing offline division of the data into various time intervals. The first 90 s were segmented to intervals of 3 s per step. Attenuation correction was performed using a map obtained from a dedicated CT imaging device. The data of each time interval were reconstructed separately resulting in 30 attenuation-corrected volumes each consisting of a set of transaxial slices. In addition, a volume containing data from the entire 5-min acquisition was generated and a region of interest (ROI) was drawn inside the left ventricular cavity. This ROI was copied to the other 30 volumes and the counts within it were measured and a left ventricular cavity time-activity curve was generated.

Results

SPECT sensitivity

Sensitivity results (Table 1) show three- to fourfold higher sensitivity of the DNM compared to S-SPECT for the cardiac phantom in air.

Energy resolution

Table 2 demonstrates an almost twofold increase in ER as measured on DNM for both ^{99m}Tc and ^{123}I isotopes and a slight increase in DNM ER for ^{201}Tl as well. Figure 4 shows the energy spectra of ^{99m}Tc for DNM and S-SPECT.

Simultaneous dual isotope ^{99m}Tc/^{123}I energy spectrum

Figure 5 shows significantly increased separation of ^{99m}Tc and ^{123}I energy peaks on DNM as contrasted with S-SPECT. In addition, the S-SPECT spectra show two fluorescence peaks for Pb at 75 and 85 keV originating at the parallel-hole collimator. Septal penetration and scatter of higher energies of ^{123}I radiopharmaceuticals and also impurities (^{124}I) contaminating the ^{123}I are also noted on S-SPECT alone and imaged as a star artefact on Fig. 6.

Table 1 Comparison of DNM and S-SPECT sensitivity. S-SPECT sensitivity, being independent of location, is measured only once

Scan phantom position	Sensitivity (counts/s per MBq)	Sensitivity (DNM)/sensitivity (S-SPECT)
DNM QFOV centre	656.8	3.19
DNM max. rate in QFOV	848.4	4.13
S-SPECT	205.7	

Table 2 ER calculated on the energy spectra curve as percentage of FWHM from peak position energy and its corresponding keV value. ER is better on DNM for all three isotopes

Isotope	ER DNM, % (keV)	ER S-SPECT, % (keV)
^{99m}Tc	5.4 (7.6)	9.4 (13.2)
^{123}I	5.8 (9.2)	9.0 (14.3)
^{201}Tl	11.7 (8.2)	13.4 (9.4)

SPECT resolution (with scatter)

The central, radial and tangential resolution (Table 3) are calculated according to NEMA NU-1 for both DNM and S-SPECT. The measurements demonstrate higher resolution for DNM compared to S-SPECT in each direction. Importantly, DNM SR for ^{201}Tl is similar to that of ^{99m}Tc. The image of the ^{201}Tl point sources (Fig. 7) clearly shows the better resolution of DNM achieved by the combined effect of higher intrinsic detector resolution, better statistics and no collimator penetration by high energy photons.

Count rate performance

Figure 8 shows linear count rate response of the DNM system up to the system limit. Maximal count rate measured was 612.2 kc/s with activity of 1,957.3 MBq (52.8 mCi) with no significant dead time losses up to the point where the computational system limit was reached with 1,994.3 MBq (53.9 mCi) dose at an actual count rate of 624.6 kc/s. In addition, the S-SPECT camera showed non-linear response with saturation and even paralysis at high count rates with a maximum of 320 kc/s, while NEMA criterion for 20% loss was reached at 210 kc/s.

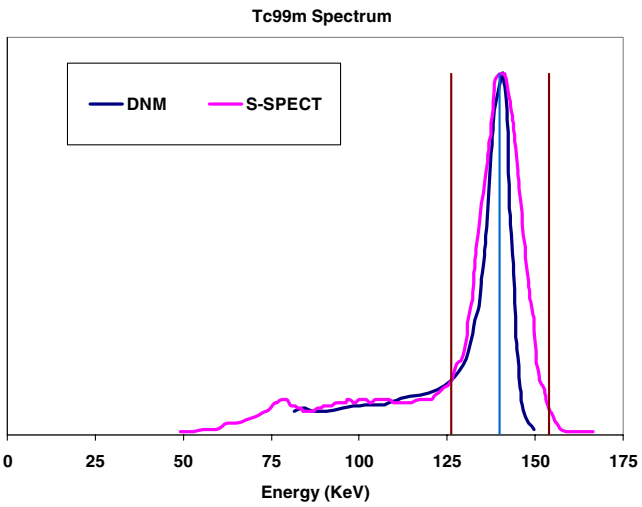

Fig. 4 Tc-99m energy spectra of DNM (*blue*) and S-SPECT (*pink*). Better energy resolution is demonstrated for the DNM (5.4%) as compared to S-SPECT (9.4%)

Phantom studies of ^{99m}Tc myocardial perfusion SPECT

Table 4 shows uniformity and contrast measurements of phantom experiments simulating low-dose rest MPS acquisitions. Overall, notwithstanding the significantly shorter acquisition time of DNM, uniformity and defect contrast trade-off is comparable or sometimes even better then S-SPECT. For yet unexplained reasons, DNM advantage was consistently more prominent for the septal defect compared to the lateral defect. A sample of reconstructed images of the anthropomorphic torso phantom is shown in Fig. 9. "Per-segment" analysis (Fig. 10) shows good correspondence in values of segmental scores between DNM and S-SPECT, with a correlation coefficient of 0.92.

Dynamic SPECT

The dynamic time-activity curve of the bolus passage through the left ventricle is shown in Fig. 11.

Discussion

Improved image characteristics

Our data show that DNM has superior sensitivity, SR and ER (Tables 1, 2 and 3) and therefore it may sustain a significant expedition and upgrade of clinical practice. The increased sensitivity is of immediate practical value since it may lead to a large reduction in acquisition time without jeopardizing image quality. Indeed, the trade-off between homogeneity of the normal segments and the defect contrast was shown in our phantom experiments to usually be comparable to DNM in spite of its shorter acquisition time (Figs. 9 and 10, Table 4). Our measurements on phantoms have now been augmented by patient data from a recent multi-centre trial [46]. Using a 1-day ^{99m}Tc-tetrofosmin rest/stress protocol in 165 patients, the authors have found that DNM provides diagnostic performance comparable to S-SPECT, on both per-patient and per-vessel analyses, while DNM acquisition time was 6- and 3.5-fold shorter than S-SPECT on rest and stress images, respectively. In addition, superior image quality was scored on DNM images. Figure 12 presents the images of one of the patients.

The enhanced ER demonstrated in DNM improves scatter rejection and thus contributes to image contrast. It can also facilitate the separate imaging of simultaneously acquired multiple different isotopes. In particular, the improved separation between the energy peaks of ^{99m}Tc and ^{123}I and the lack of ^{123}I septal penetration for the pinhole collimators (Figs. 5 and 6) are expected to lead to a variety of novel ^{99m}Tc/^{123}I dual isotope protocols. Another

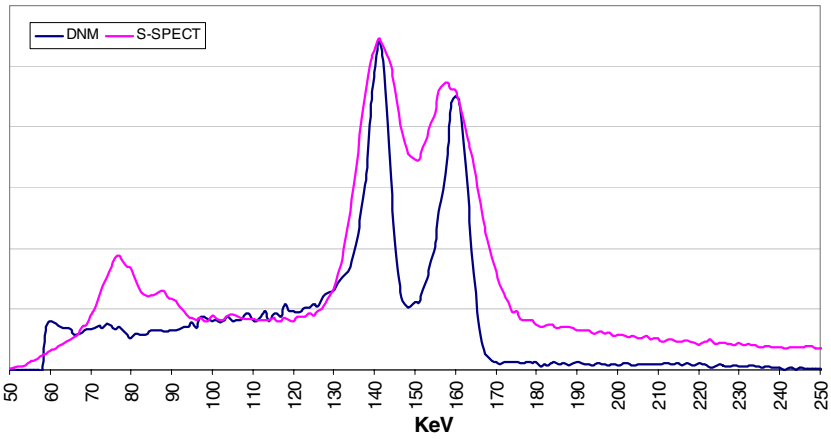

Fig. 5 Clear separation of ^{99m}Tc and ^{123}I energy peaks on DNM as contrasted with S-SPECT. In addition, the S-SPECT spectra show two fluorescence peaks for Pb at 75 and 85 keV originating at the parallel-hole collimator. Septal penetration and scatter of higher energy photons associated with the ^{123}I dose are also noted on S-SPECT alone

important feature of pixelated CZT imaging, which is advantageous for dual isotope protocols, is the common SR for all energies and isotopes. Thus, the SR for ^{201}Tl is the same as ^{99m}Tc (Table 3 and Fig. 7). Lower ^{201}Tl resolution in S-SPECT has been a source of decreased contrast on ^{201}Tl images and also a source of mismatch in the comparison of stress/rest left ventricular sizes in current ^{99m}Tc/^{201}Tl dual isotope protocols.

The DNM technology has other practical advantages; since each detector pixel has independent electronic signal readout and processing, it is therefore capable of accurate count measurements even at very high count rates, where S-SPECT cameras with their single large detector crystals fail (Fig. 8). We denoted this as "high rate count linearity". Critically, since the gantry of DNM does not move during acquisition and since all detectors are therefore acquiring the data from the source simultaneously, the projection images recorded are therefore all consistent in the time domain. That is, patient motions and isotope distributions are the same for each and every projection image submitted to the reconstruction module. This aspect of the data resembles PET imaging and its advantages; we denote it as "inherently tomographic imaging". Importantly, data acquired in a short time interval is also reconstructable, allowing even further reduction of the acquisition time when necessary, e.g. in emergency scenarios. Since images can be reconstructed on the fly, acquisition can be terminated at a preset count density or when the data becomes sufficient for diagnosis. Because of its inherent tomographic features, the DNM is capable of dynamic tomographic sampling with high temporal resolution of the left ventricular cavity and the myocardium during the initial passage of an injected bolus through the heart chambers (Fig. 11). These data are the classic input for compartmental modelling aimed at absolute CFR measurements.

Besides reducing acquisition time, the increased sensitivity of the DNM may alternatively enable a cost-saving reduction in radiopharmaceutical dosage and a corresponding reduction in patient radiation exposure, all options that contribute to flexibility and cost-effectiveness in the nuclear cardiology clinic. In addition, faster patient procedures allow more economical usage of the total dose that is prepared in advance, especially in the setup of a 1-day rest/stress protocol using ^{99m}Tc-based MPS tracers. This logistic advantage is very relevant today, due to the shortage of ^{99m}Tc generators in northern America [47]. The short acquisition times and the small footprint may enable use near the coronary care unit itself, employing long-standing protocols [48, 49] for MPS in scenarios of acute coronary syndrome. Alternatively, scientists and clinicians concerned with the best image quality may utilize the DNM sensitivity to acquire higher statistics still in a relatively short time. For example, more precise gated acquisition with more and hence shorter gate intervals may allow the algorithmic creation of de-blurred

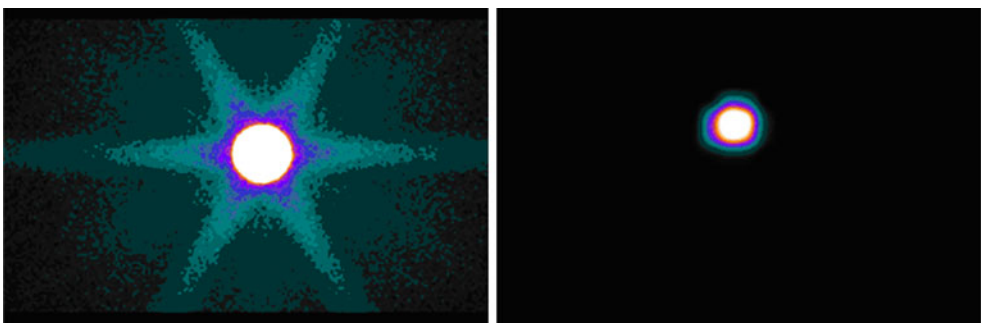

Fig. 6 ^{123}I images. *Left*: planar image from S-SPECT system demonstrates a "star effect" due to parallel-hole collimator septal penetration and scatter of higher energy photons associated with the ^{123}I. *Right*: "planar" image on a single collimator-detector module of DNM system has no "star effect"

Table 3 Central, tangential and radial resolution calculated according to NEMA NU-1 for both DNM and S-SPECT for point sources filled with ^{99m}Tc or ^{201}Tl

DNM		
	^{201}Tl	^{99m}Tc
5.8	6.1	Central (mm)
2.9	3.1	Tangential (mm)
4.0	4.3	Radial (mm)
S-SPECT		
	^{201}Tl	^{99m}Tc
13.7	10.9	Central (mm)
11.7	7.5	Tangential (mm)
15.4	10.9	Radial (mm)

perfusion images free of both respiratory motion and cardiac motion artefacts [50, 51]. Such de-blurring is an essential preliminary step before any hardware improvement of SR can become effective. In addition, an increased number of gates may be used for new applications that are related to myocardial electrical conduction and contractility that are currently being developed [52]. Patient motion itself and its consequential artefacts may be reduced because of increased patient comfort and cooperation during the short acquisitions. Furthermore the inherent tomographic imaging may potentially enable 3-D patient motion correction including rotation, while S-SPECT methods can usually directly account only for translations. In addition, S-SPECT artefacts resulting from temporal inconsistency, such as the "upward creep" artefact, which is created when the heart gradually moves up during the S-SPECT camera rotation [53, 54], may be less of a problem with the temporally consistent DNM projections.

The DNM higher sensitivity and its improved SR and ER for ^{201}Tl (Tables 2 and 3 and Fig. 7) are expected to significantly improve imaging with this isotope. This perfusion tracer has known physiological advantages [55], but yields poorer statistics, because of its longer half-life and lower energy. Even though useful gated ^{201}Tl images have been obtained with modern S-SPECT cameras [56, 57], usage had been limited by image quality. Since ^{201}Tl acquisition commences almost immediately after stress, improved gating with ^{201}Tl, using DNM, is expected to result in increased detection of myocardial stunning, which is indicative of severe CAD. Similarly, improved image quality is expected to support improved characterization of myocardial viability when using 24- or even 48-h delayed images, the latter being impractical with S-SPECT. Interestingly, improving the quality of ^{201}Tl images has recently become more pertinent due to the shortage of ^{99m}Tc generators in northern America [47, 58]. Figure 13 shows images of a patient study using a ^{201}Tl protocol demonstrating comparable images of DNM and S-SPECT in spite of much shorter acquisition time on DNM.

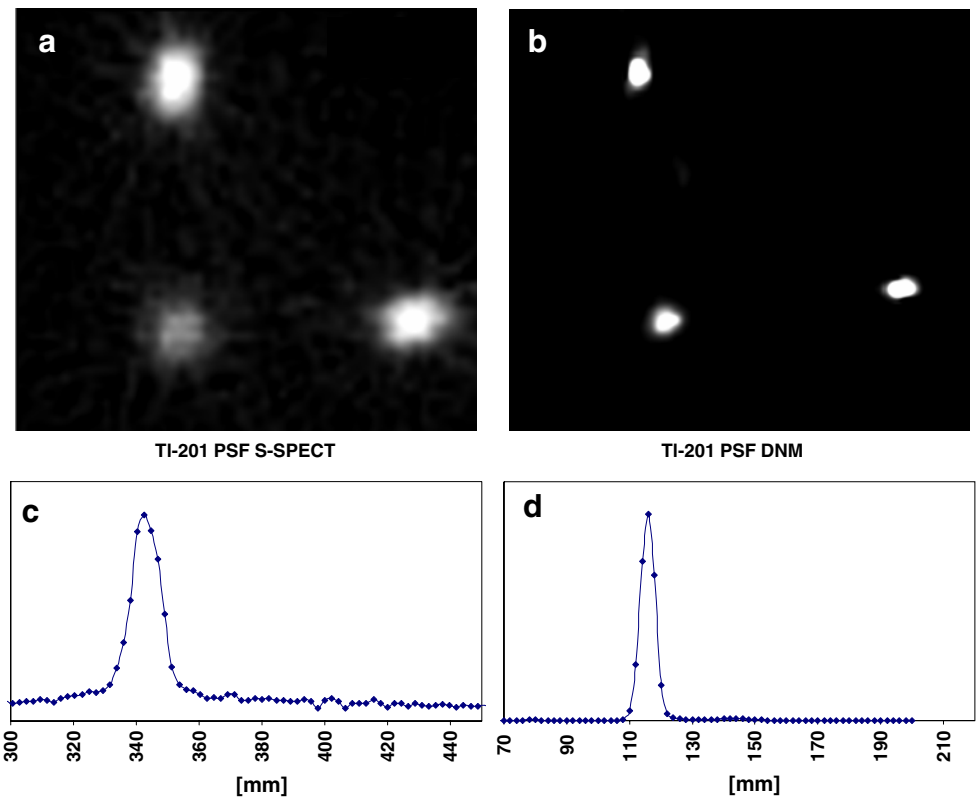

Fig. 7 ^{201}Tl point sources as imaged on a dedicated conventional cardiac SPECT camera (**a**) and DNM (**b**), clearly demonstrating the higher resolution of the DNM. In addition corresponding line profiles reveal the degrading effect of septal penetration of the parallel hole collimator on S-SPECT resolution (**c**), while no septal penetration is evident on DNM (**d**)

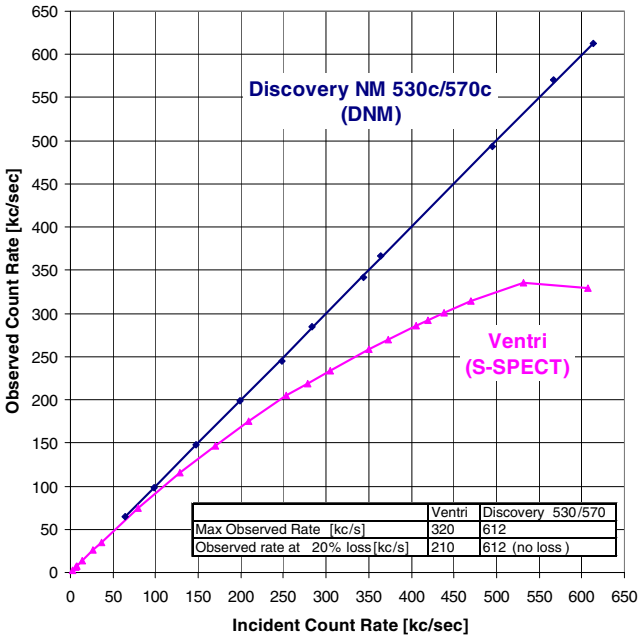

Fig. 8 Count rate performance with both systems operating at optimal mode for high count rate using ^{99m}Tc sources. According to NEMA guidelines the incident rate is determined by assuming that it is equal to the rate observed on the camera at low doses, while higher doses are normalized accordingly. The curves demonstrate linear count rate response of the DNM system (*blue line*) up to the system computer limit and non-linear response with saturation and even paralysis of S-SPECT (*pink line*). The maximal rate achieved with DNM is almost twice of what can be achieved with S-SPECT. No count loss is noted with DNM, while NEMA criterion for 20% loss was reached at 210 kc/s on S-SPECT

Potential limitations of the DNM should also be considered; a major theoretical concern is incomplete sampling of data. This may occur since the DNM collimation is concentrated on the heart vicinity and may unevenly sample extracardiac activity. Our phantom studies that included various degrees of liver activity, as well as a recent multi-centre clinical trial, did not reveal explicit problems, so far. However, this potential theoretical limitation should be addressed by special studies designed to evaluate the actual effect, and especially for optimizing the accuracy of quantitative dynamic measurements. Another limitation of our study relates to the difficulty in comparing such radically different technologies, especially when standardized quality control procedures, like NEMA, do not exist for DNM. In particular, the SR measurements (Table 3) had to be done using different reconstruction algorithms, FBP for S-SPECT and MLEM for DNM. Since measurements were performed on point sources, they may not ideally reflect the actual resolution that would be achieved in real-world clinical scenarios.

Expedited new protocols

In addition to shorter acquisition times, the DNM may allow fast MPS protocols with back-to-back stress/rest gated SPECT acquisitions, significantly shorter than 1 h, while occupying the camera for no more than 15 min total. There are at least three different ways. The first possibility is using stress/rest subtraction protocols. Such protocols shall begin with a stress acquisition. If stress data are abnormal, another dose is injected while the patient is resting within the camera, followed by another acquisition 3 min later and then image subtraction. Better subtraction is expected with DNM short acquisition because of the reduction in patient motion and myocardial shift. The 3-min wait for the second acquisition is similar to the time needed for patient positioning for a second separate acquisition in S-SPECT. Moreover, this time may be used for dynamic gated acquisition of the injected bolus.

A second fast protocol that may be facilitated by DNM is simultaneous dual isotope imaging, for example ^{99m}Tc and ^{201}Tl following stress and rest injection, respectively. Such protocols have been evolving for S-SPECT [59–61] and may now reach maturity, because of the available DNM detector performance.

A third fast MPS protocol is the reconsideration of tracers that are rapidly washed from the myocardium because of the high sensitivity and simultaneous views data. A very interesting tracer is ^{99m}Tc-boronic acid teboroxime (BATO), an FDA-approved tracer that is close to Saperstein's [62] definition of an ideal myocardial perfusion tracer. BATO's extraction fraction is higher than

Table 4 Results of uniformity and contrast measurements for phantom experiments simulating low-dose rest part of MPS acquisition, including lateral and septal wall defect inserts. Each measurement represents a series of ten phantom acquisitions performed sequentially on DNM and S-SPECT (Ventri). Overall, notwithstanding the significantly shorter acquisition time of DNM, uniformity and defect contrast trade-off are comparable to S-SPECT

	Male phantom configuration mean (SD)		Female phantom configuration mean (SD)	
	DNM	S-SPECT	DNM	S-SPECT
NSD, %	12.5 (1.0)	13.6 (1.35)	14.9 (0.98)	17.5 (2.55)
Lat EC, %	38.5 (4.75)	30.5 (8.5)	37.5 (6.35)	42.3 (6.05)
Sep EC, %	28.5 (4.1)	14.2 (5.55)	33.8 (5.8)	20.3 (10.55)

SD standard deviation, *NSD* normalized standard deviation, *Lat* lateral wall defect, *EC* effective contrast, *Sep* septal wall defect

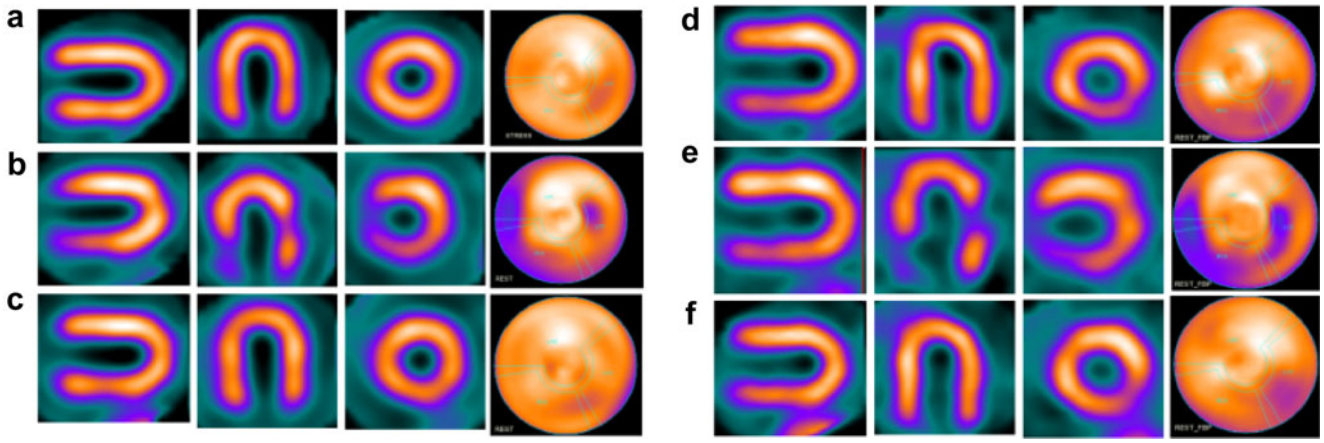

Fig. 9 Samples of phantom comparisons: tomographic slices and corresponding polar plots obtained using a low-dose rest acquisition. *Left panel*: DNM (3-min acquisition). *Right panel*: S-SPECT (15-min acquisition). *Upper row*: male configuration without a defect. *Middle row*: female configuration with medium-sized breast inserts and with perfusion defects in the septal and lateral walls. *Lower row*: male configuration with hot liver and without a defect. Images are quite comparable in spite of fivefold shorter acquisition time on the DNM

those of ^{201}Tl or ^{99m}Tc tracers and its myocardial uptake remains a near-linear function of flow even at high flow rates [63, 64]. Its initial myocardial uptake as well as its segmental washout rate correlate well with coronary blood flow, providing two different targets for quantitative measurements [23, 65]. Moreover, the high myocardial extraction and rapid biological clearance allow for very short stress/rest protocols [66]. The differential washout of BATO may produce filling of stress perfusion defect within a few minutes of early delayed images in a high percentage of patients, potentially eliminating the need for a second rest injection [67]. In spite of BATO's unique qualities, it never gained wide usage. Acquisition and tomographic reconstruction of rapidly changing myocardial distribution with rotating S-SPECT technology is prone to inconsistency errors. Another issue was high concentration in the liver [68]. These barriers led to the disappearance of BATO from mainstream nuclear cardiology practice [69]. A recent simulation study [70] showed that a stationary SPECT camera might suit dynamic BATO studies better than a rotational S-SPECT camera. Indeed, with DNM, using adenosine or regadenoson [71] stress, with BATO injected when the patient is inside the camera, a high count rate stress/redistribution study may be completed in less than 10 min. If both perfusion and function are normal or if perfusion is abnormal but redistribution is noted in all defects, a separate rest BATO injection may be omitted. Otherwise, 15 min later and onward, a separate rest injection followed by a 5-min acquisition may be performed, completing a back-to-back stress/rest study in just about 30 min and occupying the camera for about 15 min.

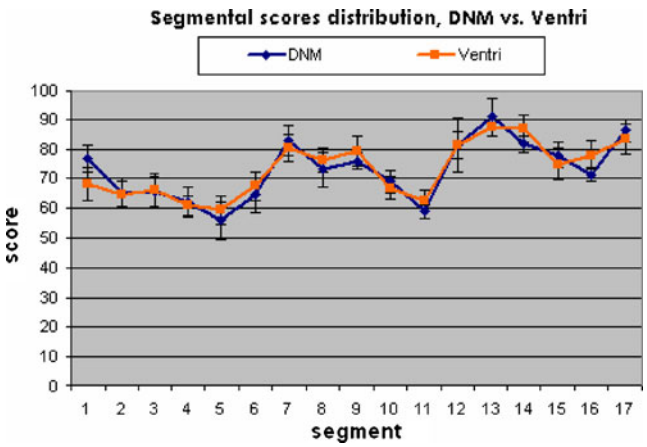

Fig. 10 Distribution of segmental scores for a series of ten uniform phantoms acquired under conditions mimicking low-dose rest acquisition. *Blue*: DNM short acquisition time. *Orange*: S-SPECT (Ventri) with longer acquisition time. *Error bars* represent two standard deviation values showing variability within corresponding series. Most segments show comparable mean scores and the differences between the scores of the two modalities are similar to their intrinsic variability

Hybrid non-invasive CAD diagnosis: "the best of both worlds"

Currently, accurate structural imaging of CAD can be obtained non-invasively with multidetector computed X-ray tomography (MDCT) [72]. However, when the ability of MDCT to detect ischaemia was tested against MPS, several studies [31, 73, 74] have found that while MDCT is consistently associated with outstanding negative predictive values (usually >90%) it provides only mediocre positive predictive values (29–44%). The ultimate value of a CAD imaging modality does depend on its ability to optimally assign the best treatment strategy to patients, especially differentiating between medical therapy and invasive revascularization [75]. The ability of MDCT to meet this challenge is problematic, given that even invasive diagnostic

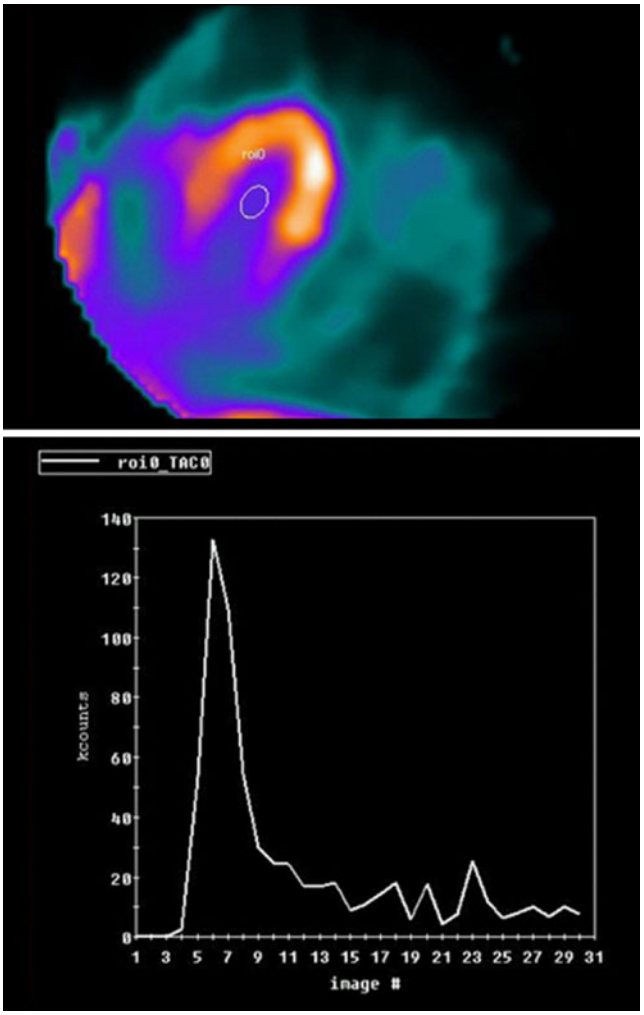

Fig. 11 *Upper panel*: ROI within the left ventricular cavity. *Lower panel*: dynamic time-activity curve of the same ROI, reflecting the first 90 s of bolus passage

angiography, the gold standard of coronary anatomy, is suboptimal for the task [76, 77]. Since DNM is also a small footprint camera and its short acquisition time resonates well with MDCT acquisition time, their optional usage in concert may help to efficiently arrive at a comprehensive diagnosis. This hybrid design concept (Fig. 1) is a continuation of "the best of both worlds" idea that underlined the creation of the Hawkeye—the archetypical, first clinical SPECT/PET/CT [78]. In the context of CAD, such hybridization may evolve into a new type of diagnostic cardiac lab, where the decision to revascularize is made based on non-invasive procedures that are physically, temporally and conceptually separated from the invasive action.

Dynamic SPECT and the comeback of "first pass"

DNM high sensitivity combined with its dynamic SPECT capabilities may cause renewed interest in radionuclide angiocardiography, traditionally known as "first pass" (FP) [79], however, in a new tomographic form. The use of FP, one of the first breakthroughs in the history of nuclear medicine, has almost vanished in spite of its many advantages. FP acquisition time is less than 1 min, while it provides information on the volume and motion of each heart chamber and a measurement of its ejection fraction (EF). In particular, it gives more accurate information on the right ventricle than available with equilibrium gated angiocardiography (MUGA scan) [80]. FP can be repeated immediately, using tracers that rapidly disappear from the blood pool or ultra-short-lived radionuclides such as ^{191m}Ir [81], for imaging multiple interventions. FP has been shown to provide important complementary information to SPECT MPS [82]. Nevertheless, its usage in the planar mode had declined for a variety of reasons. In order to reduce the errors that resulted from planar background subtraction, each cardiac chamber had its own imaging view and only a few seconds of optimal time window for acquisition. Therefore the information was based on a few cardiac cycles only. A "good bolus" was required for reliable data and was often non-obtainable in patients with damaged veins due to chemotherapy, and in patients with reduced cardiac function. Other serious problems were caused by the count rate limitations of the Anger camera. On the one hand, the count rate from a large dose could exceed the linear range of the counting electronics, yet, on the other hand, basic gated frames were typically acquired in approximately 0.1 s and had very few signal counts which caused errors in the detection of the cardiac wall motion. As described earlier the DNM camera has the technological assets to overcome those technical limitations. In addition, since DNM is tomographic, background should not be a major problem and acquisition can be continued for unlimited cardiac cycles and a "good bolus" may not be essential.

Evolutionary perspective: the potential for increased resolution

The future of DNM may be the most intriguing question since the design can be optimized in a variety of directions. Since nuclear cardiology is concerned today mainly with imaging of relatively large "cold spots", of the order of 1 cm or more, the current optimization achieves significant reduction in acquisition time with conservative improvements in SR (Tables 1 and 3). In addition, currently, any major improvement of SR would be masked by cardiac and respiratory motions. However, the imaging entitlement of the new technology could equally be used to achieve very high SR if needed and from an evolutionary perspective, resolution improvement should be given high priority in the years ahead. In fact, DNM core technology was developed in the microSPECT environment that has recently achieved a resolution of 400 μm, while main-

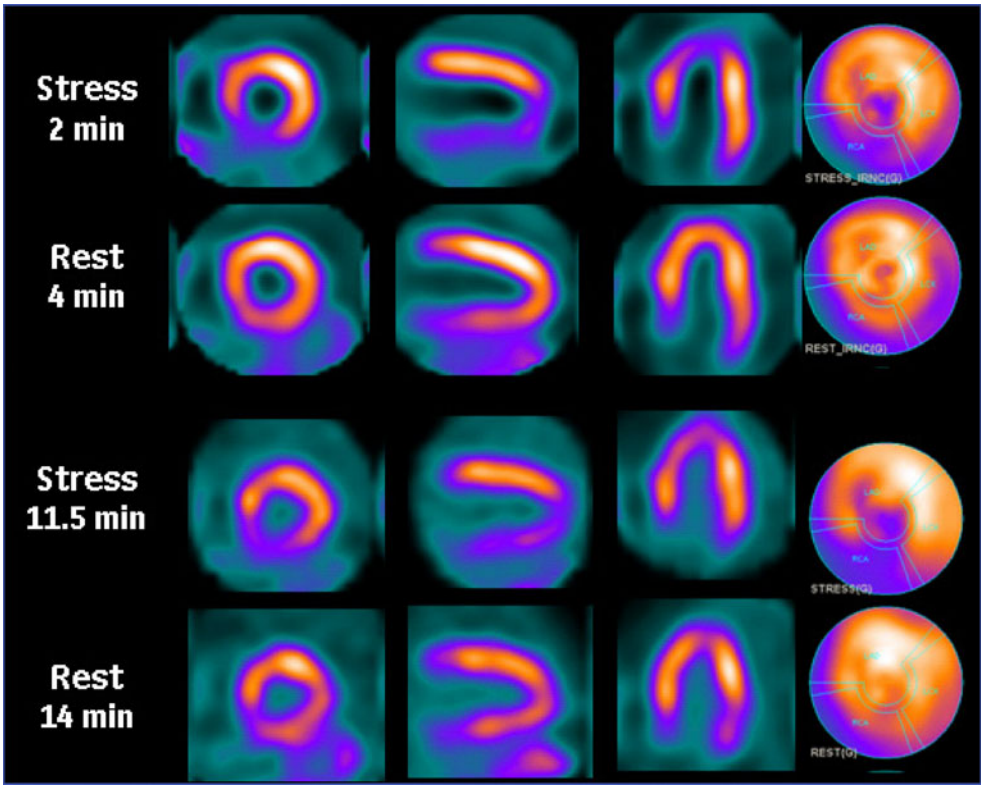

Fig. 12 A 1-day ^{99m}Tc-tetrofosmin study. *Upper two rows*: DNM images employing short acquisition times. *Lower two rows*: images of the same patient acquired by conventional dedicated cardiac SPECT with significantly longer acquisition times. Images are comparable and both are compatible with inferoseptal wall ischaemia of the left ventricular wall extending to the apical area. Courtesy of the Department of Nuclear Medicine, Rambam Hospital, Israel

taining sufficient sensitivity [36]. Thus, the nuclear cardiology community may witness in the near future an evolving line of cameras with continuously improving SR. The prospect of using gated MPS and/or MDCT data for improved resolution recovery or for SPECT motion tracking and de-blurring seems to be a critical next step [50, 51]. Beyond that obligatory step, an increase in resolution to allow differentiation between subendocardial—and subepicardial—myocardium may benefit classic MPS. An increase in ultimate resolution would also enable a more accurate CFR measurement by allowing a reduction of spillover effects from the blood pool into the myocardium

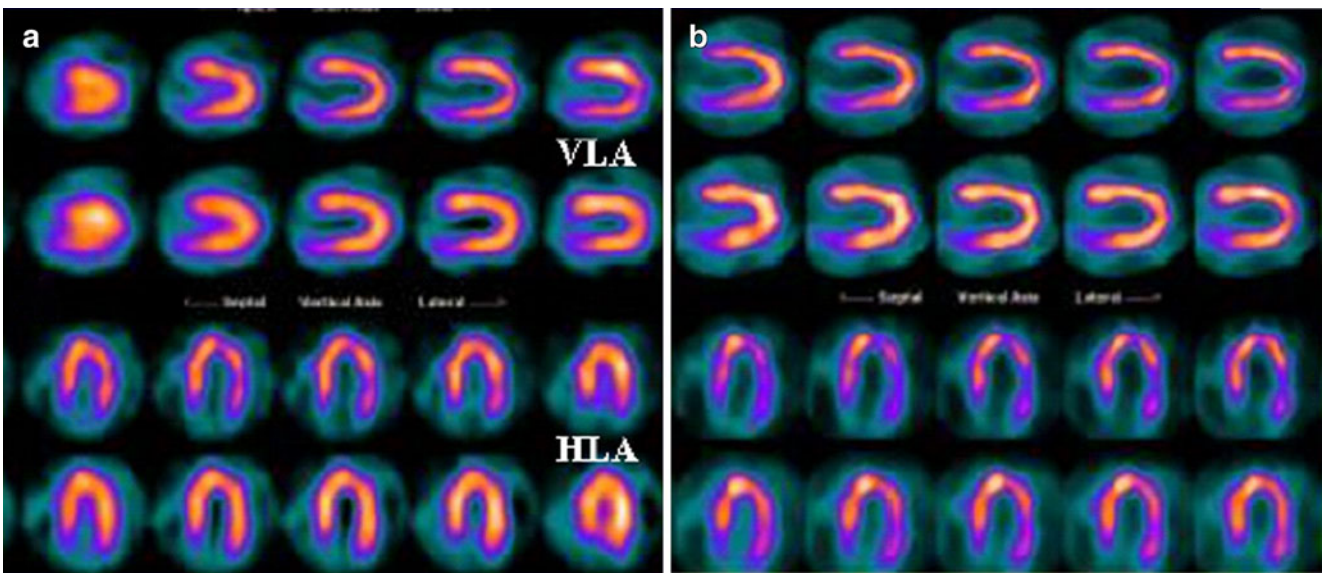

Fig. 13 A treadmill stress/rest ^{201}Tl study. **a** Conventional SPECT images employing 20 min acquisition for each stress or rest data set. **b** DNM image employing only 6 min acquisition for each data set. Myocardial ischaemia of the inferolateral wall of the left ventricle is noted on both modalities. *VLA* vertical long axis, *HLA* horizontal long axis. Courtesy of Dr. Iftikhar Ali from Ottawa Heart Institute, Canada

and vice versa, as both effects are contaminating the respective time-activity curves.

We also envision that in the near future increased resolution will be a key factor as nuclear cardiology matures within molecular imaging. While the importance of PET imaging will continue, unlike PET, SPECT is capable of simultaneous multiple isotope imaging and additionally, in theory, a better SR may ultimately be achieved with SPECT. Since identifying individual patients with vulnerable plaques at high risk for rupture is a central challenge, various studies including first clinical trials have been using different tracers for "hot spot" plaque imaging studies [83]. Other research targets include imaging of left ventricular remodelling, angiogenesis, apoptosis and hypoxia, gene expression, and stem cell therapy, to delineate a few. Thus we can predict a steady evolution of nuclear cardiology beyond the assessment of myocardial perfusion, towards the characterization of molecular events. Since DNM technology and recent innovative camera designs [84] have great potential for further improvement, they may turn out to be the first evolutionary step in linking molecular biology science and clinical cardiology.

Conclusion

The DNM, an ultra-fast cardiac SPECT camera, was created to answer the call of current evolutionary challenges in nuclear cardiology. It features high sensitivity as well as improved SR, temporal resolution and ER. It enables reduction of acquisition time and fast protocols. Importantly, it is inherently tomographic imaging and features high count rate linearity and therefore is potentially capable of dynamic 3-D acquisition. The DNM is designed to optionally work with MDCT, together comprising a system of comprehensive, non-invasive, functional and anatomical imaging for the management of CAD.

Acknowledgement This article is dedicated to the memory of Bruce Hasegawa; many of the ideas contained herein were inspired by his near and far presence.

Conflicts of interest The first author (MB) was consulting GE Healthcare during the DNM project. All the other authors are employees of GE.

References

1. Russell 3rd RR, Zaret BL. Nuclear cardiology: present and future. Curr Probl Cardiol 2006;31(9):557–629.
2. Hachamovitch R, Berman DS, Kiat H, Cohen I, Friedman JD, Shaw LJ. Value of stress myocardial perfusion single photon emission computed tomography in patients with normal resting electrocardiograms: an evaluation of incremental prognostic value and cost-effectiveness. Circulation 2002;105:823–9.
3. Underwood SR, Shaw LJ, Anagnostopoulos C, Cerqueira M, Ell PJ, Flint J, et al. Myocardial perfusion scintigraphy and cost effectiveness of diagnosis and management of coronary heart disease. Heart 2004;90 Suppl 5:v34–6.
4. Beller GA. First annual Mario S. Verani, MD, memorial lecture: clinical value of myocardial perfusion imaging in coronary artery disease. J Nucl Cardiol 2003;10:529–42.
5. Marcassa C, Bax JJ, Bengel F, Hesse B, Petersen CL, Reyes E, et al. Clinical value, cost-effectiveness, and safety of myocardial perfusion scintigraphy: a position statement. Eur Heart J 2008;29 (4):557–63.
6. US Imaging Market Guide, Arlington Medical Resources, Malvern (PA) (2007).
7. Ficaro EP, Corbett JR. Advances in quantitative perfusion SPECT imaging. J Nucl Cardiol 2004;11(1):62–70.
8. Sciagrà R, Leoncini M. Gated single-photon emission computed tomography. The present-day "one-stop-shop" for cardiac imaging. Q J Nucl Med Mol Imaging 2005;49(1):19–29.
9. Lin GS, Hines HH, Grant G, Taylor K, Ryals C. Automated quantification of myocardial ischemia and wall motion defects by use of cardiac SPECT polar mapping and 4-dimensional surface rendering. J Nucl Med Technol 2006;34(1):3–17.
10. Seo Y, Mari C, Hasegawa BH. Technological development and advances in single-photon emission computed tomography/computed tomography. Semin Nucl Med 2008;38(3):177–98.
11. Pear R. Health spending exceeded record $2 trillion in 2006 New York Times. Health. 2008 Jan 8
12. Poisal A, Truffer C, Smith S, Sisko A, Cowan C, Keehan S, et al. Health spending projections through 2016: modest changes obscure part D's impact. Health Aff (Millwood) 2007;26:w242–53.
13. Report to the Congress: Medicare payment policy, Medicare Payment Advisory Commission, Washington, DC 2007.
14. Lucas FL, DeLorenzo MA, Siewers AE, Wennberg DE. Temporal trends in the utilization of diagnostic testing and treatments for cardiovascular disease in the United States, 1993–2001. Circulation 2006;113:374–9.
15. Case J, Cullom S, Bateman T. Myocardial perfusion single-photon emission computed tomography attenuation correction. In: Iskandrian AE, Verani MS, editors. Nuclear cardiac imaging: principles and applications. 3rd ed. New York: Oxford University; 2003. p. 106–20.
16. Aarnoudse WH, Botman KJ, Pijls NH. False-negative myocardial scintigraphy in balanced three-vessel disease, revealed by coronary pressure measurement. Int J Cardiovasc Intervent 2003;5:67–71.
17. Dahlberg S, Leppo J. Risk stratification of the normal perfusion scan: does normal stress perfusion always mean very low risk? J Nucl Cardiol 2003;10:87–91.
18. Lima RSL, Watson DD, Goode AR, Siadaty MS, Ragosta M, Beller GA, et al. Incremental value of combined perfusion and function over perfusion alone by gated SPECT myocardial perfusion imaging for detection of severe three-vessel coronary artery disease. J Am Coll Cardiol 2003;42:64–70.
19. Ragosta M, Bishop AH, Lipson LC, Watson DD, Gimple LW, Sarembock IJ, et al. Comparison between angiography and fractional flow reserve versus single-photon emission computed tomographic myocardial perfusion imaging for determining lesion significance in patients with multivessel coronary disease. Am J Cardiol 2007;99:896–902.
20. Travin MI. Is it possible for myocardial perfusion imaging to avoid missing any patients with high-risk coronary disease? J Nucl Cardiol 2007;14(4):492–6.

21. Berman DS, Kang X, Slomka PJ, Gerlach J, de Yang L, Hayes SW, et al. Underestimation of extent of ischemia by gated SPECT myocardial perfusion imaging in patients with left main coronary artery disease. J Nucl Cardiol 2007;14:521–8.
22. Takaro T, Hultgren HN, Lipton MJ, Detre KM. The VA cooperative randomized study of surgery for coronary arterial occlusive disease II. Subgroup with significant left main lesions. Circulation 1976;54(Suppl):III107–17.
23. Smith AM, Gullberg GT, Christian PE. Experimental verification of technetium 99m-labeled teboroxime kinetic parameters in the myocardium with dynamic single-photon emission computed tomography: reproducibility, correlation to flow, and susceptibility to extravascular contamination. J Nucl Cardiol 1996;3(2):130–42.
24. Di Bella EV, Ross SG, Kadrmas DJ, Khare HS, Christian PE, McJames S, et al. Compartmental modeling of technetium-99m-labeled teboroxime with dynamic single-photon emission computed tomography: comparison with static thallium-201 in a canine model. Invest Radiol 2001;36(3):178–85.
25. Gullberg GT, Di Bella EV, Sinusas AJ. Estimation of coronary flow reserve: can SPECT compete with other modalities? J Nucl Cardiol 2001;8(5):620–5.
26. Iida H, Eberl S, Kim KM, Tamura Y, Ono Y, Nakazawa M, et al. Absolute quantitation of myocardial blood flow with (201)Tl and dynamic SPECT in canine: optimisation and validation of kinetic modelling. Eur J Nucl Med Mol Imaging 2008;35 (5):896–905.
27. Petretta M, Soricelli A, Storto G, Cuocolo A. Assessment of coronary flow reserve using single photon emission computed tomography with technetium 99m-labeled tracers. J Nucl Cardiol 2008;15(3):456–65.
28. Yoshinaga K, Katoh C, Noriyasu K, Iwado Y, Furuyama H, Ito Y, et al. Reduction of coronary flow reserve in areas with and without ischemia on stress perfusion imaging in patients with coronary artery disease: a study using oxygen 15-labeled water PET. J Nucl Cardiol 2003;10:275–83.
29. Parkash R, deKemp RA, Ruddy TD, Kitsikis A, Hart R, Beauschene L, et al. Potential utility of rubidium 82 PET quantification in patients with 3-vessel coronary artery disease. J Nucl Cardiol 2004;11:440–9.
30. Di Carli MF, Hachamovitch R. Should PET replace SPECT for evaluating CAD? The end of the beginning. J Nucl Cardiol 2006;13(1):2–7.
31. Di Carli MF, Hachamovitch R. New technology for noninvasive evaluation of coronary artery disease. Circulation 2007;115 (11):1464–80.
32. Gould KL. Positron emission tomography in coronary artery disease. Curr Opin Cardiol 2007;22(5):422–8.
33. Di Carli MF, Dorbala S, Meserve J, El Fakhri G, Sitek A, Moore SC. Clinical myocardial perfusion PET/CT. J Nucl Med 2007;48 (5):783–93.
34. deKemp RA, Yoshinaga K, Beanlands RS. Will 3-dimensional PET-CT enable the routine quantification of myocardial blood flow? J Nucl Cardiol 2007;14(3):380–97.
35. Vogel RA, Kirch D, LeFree M, Steele P. A new method of multiplanar emission tomography using a seven pinhole collimator and an Anger scintillation camera. J Nucl Med 1978;19 (6):648–54.
36. Beekman F, van der Have F. The pinhole: gateway to ultra-high-resolution three-dimensional radionuclide imaging. Eur J Nucl Med Mol Imaging 2007;34(2):151–61.
37. Funk T, Kirch DL, Koss JE, Botvinick E, Hasegawa BH. A novel approach to multipinhole SPECT for myocardial perfusion imaging. J Nucl Med 2006;47(4):595–602.
38. Funk T, Després P, Barber WC, Shah KS, Hasegawa BH. A multipinhole small animal SPECT system with submillimeter spatial resolution. Med Phys 2006;33(5):1259–68.
39. Franc BL, Acton PD, Mari C, Hasegawa BH. Small-animal SPECT and SPECT/CT: important tools for preclinical investigation. J Nucl Med 2008;49(10):1651–63.
40. Blevis I, Tsukerman L, Volokh L, Hugg J, Jansen F, Bouhnik JP. CZT gamma camera with pinhole collimator: detector efficiency. Abstract: Nuclear Science Symposium 2008. IEEE 19–25 Oct 2008
41. Blevis I, Tsukerman L, Volokh L, Hugg J, Jansen F, Bouhnik JP. CZT gamma camera with pinhole collimator: spectral measurements. Abstract: Nuclear Science Symposium 2008. IEEE 19–25 Oct 2008.
42. Hebert T, Leahy R. A generalized EM algorithm for 3D Bayesian reconstruction from Poisson data using Gibbs priors. IEEE Trans Med Imaging 1989;8:194–202.
43. Green PJ. Bayesian reconstructions from emission tomography data using a modified EM algorithm. IEEE Trans Med Imaging 1990;9(1):84–93.
44. Volokh L, Lahat C, Binyamin E, Blevis I. Myocardial perfusion imaging with an ultra-fast cardiac SPECT camera—a phantom study. Nuclear Science Symposium Conference Record, 2008. NSS '08. IEEE 19–25 Oct 2008. p. 4636–4639.
45. Cerqueira MD, Weissman NJ, Dilsizian V, Jacobs AK, Kaul S, Laskey WK, et al. Standardized myocardial segmentation and nomenclature for tomographic imaging of the heart: a statement for healthcare professionals from the Cardiac Imaging Committee of the Council on Clinical Cardiology of the American Heart Association. Circulation 2002;105(4):539–42.
46. Esteves FP, Raggi P, Folks RD, Keidar Z, Askew JW, Rispler S, et al. Novel solid-state-detector dedicated cardiac camera for fast myocardial perfusion imaging: multicenter comparison with standard dual detector cameras. J Nucl Cardiol 2009;16:927–34.
47. Einstein AJ. Breaking America's dependence on imported molybdenum. JACC Cardiovasc Imaging 2009;2(3):369–71.
48. Christian TF. The use of perfusion imaging in acute myocardial infarction: applications for clinical trials and clinical care. J Nucl Cardiol 1995;2(5):423–36.
49. Sinusas AJ. Assessment of reperfusion after acute myocardial infarction: is there a role for acute technetium 99m-teboroxime imaging? J Nucl Cardiol 1996;3(1):82–5.
50. Slomka PJ, Nishina H, Berman DS, Kang X, Akincioglu C, Friedman JD, et al. "Motion-frozen" display and quantification of myocardial perfusion. J Nucl Med 2004;45(7):1128–34.
51. Kovalski G, Israel O, Keidar Z, Frenkel A, Sachs J, Azhari H. Correction of heart motion due to respiration in clinical myocardial perfusion SPECT scans using respiratory gating. J Nucl Med 2007;48(4):630–6.
52. Chen J, Henneman MM, Trimble MA, Bax JJ, Borges-Neto S, Iskandrian AE, et al. Assessment of left ventricular mechanical dyssynchrony by phase analysis of ECG-gated SPECT myocardial perfusion imaging. J Nucl Cardiol 2008;15(1):127–36.
53. Friedman J, Van Train K, Maddahi J, Rozanski A, Prigent F, Bietendorf J, et al. "Upward creep" of the heart: a frequent source of false-positive reversible defects during thallium-201 stress-redistribution SPECT. J Nucl Med 1989;30(10):1718–22.
54. Bok BD, Bice AN, Clausen M, Wong DF, Wagner HN. Artifacts in camera based single photon emission tomography due to time activity variation. Eur J Nucl Med 1987;13:439–42.
55. Strauss HW, Bailey D. Resurrection of thallium-201 for myocardial perfusion imaging. JACC Cardiovasc Imaging 2009;2(3):283–5.
56. Germano G, Erel J, Kiat H, Kavanagh PB, Berman DS. Quantitative LVEF and qualitative regional function from gated thallium-201 perfusion SPECT. J Nucl Med 1997;38(5):749–54.
57. Santiago JF, Heiba SI, Jana S, Mirzaitehrane M, Dede F, Abdel-Dayem HM. Transient ischemic stunning of the myocardium in stress thallium-201 gated SPET myocardial perfusion imaging: segmental analysis of myocardial perfusion, wall motion and wall thickening changes. Eur J Nucl Med Mol Imaging 2002;29 (8):979–83.

58. Dilsizian V, Narula J. Seeking remedy for Molly's woe: time for a thallium pill? JACC Cardiovasc Imaging 2009;2(3):375–7.
59. Weinmann P, Faraggi M, Moretti JL, Hannequin P. Clinical validation of simultaneous dual-isotope myocardial scintigraphy. Eur J Nucl Med Mol Imaging 2003;30(1):25–31.
60. Brown JK, Tang HR, Hattner RS, Bocher M, Ratzlaff NW, Kadkade PP, et al. Intrinsic dual-energy processing of myocardial perfusion images. J Nucl Med 2000;41(7):1287–97.
61. Steele PP, Kirch DL, Koss JE. Comparison of simultaneous dual-isotope multipinhole SPECT with rotational SPECT in a group of patients with coronary artery disease. J Nucl Med 2008;49(7):1080–9.
62. Sapirstein LA. Fractionation of the cardiac output of rats with isotopic potassium. Circ Res 1956;4(6):689–92.
63. Beanlands R, Muzik O, Nguyen N, Petrey N, Schwaiger M. The relationship between myocardial retention of technetium-99m teboroxime and myocardial blood flow. J Am Coll Cardiol 1992;20:712–9.
64. Johnson LL. Myocardial perfusion imaging with technetium-99m-teboroxime. J Nucl Med 1994;35(4):689–92.
65. Chiao P-C, Ficaro EP, Dayanikli F, Rogers WL, Schwaiger M. Compartmental analysis of technetium-99m-teboroxime kinetics employing fast dynamic SPECT at rest and stress. J Nucl Med 1994;35:1265–73.
66. Seldin DW, Johnson LL, Blood DK, Muschel MJ, Smith KF, Wall RM, et al. Myocardial perfusion imaging with technetium-99m SQ30217: comparison with thallium-201 and coronary anatomy. J Nucl Med 1989;30(3):312–9.
67. Phillips DJ, Henneman RA, Merhige ME. Rapid diagnosis of coronary disease using dipyridamole and teboroxime washout imaging [abstract]. J Am Coll Cardiol 1994;23:255.
68. Chua T, Kiat H, Germano G, Takemoto K, Fernandez G, Biasio Y, et al. Rapid back to back adenosine stress/rest technetium-99m teboroxime myocardial perfusion SPECT using a triple-detector camera. J Nucl Med 1993;34(9):1485–93.
69. Burns RJ. Technetium 99m-labeled teboroxime: death in utero, infanticide, or failure to thrive? J Nucl Cardiol 1995;2(1):88–91.
70. Roberts J, Maddula R, Clackdoyle R, DiBella E, Fu Z. The effect of acquisition interval and spatial resolution on dynamic cardiac imaging with a stationary SPECT camera. Phys Med Biol 2007;52 (15):4525–40.
71. Mahmarian JJ, Cerqueira MD, Iskandrian AE, Bateman TM, Thomas GS, Hendel RC, et al. Regadenoson induces comparable left ventricular perfusion defects as adenosine: a quantitative analysis from the ADVANCE MPI 2 trial. JACC Cardiovasc Imaging 2009;2(8):959–68.
72. Leber W, Knez A, von Ziegler F, Becker A, Nikolaou K, Paul S, et al. Quantification of obstructive and nonobstructive coronary lesions by 64-slice computed tomography: a comparative study with quantitative coronary angiography and intravascular ultrasound. J Am Coll Cardiol 2005;46:147–54.
73. Dorbala S, Hachamovitch DR, Di Carli MF. Myocardial perfusion imaging and multidetector computed tomographic coronary angiography: appropriate for all patients with suspected coronary artery disease? J Am Coll Cardiol 2006;48:2515–7.
74. Gaemperli O, Schepis T, Valenta I, Koepfli P, Husmann L, Scheffel H, et al. Functionally relevant coronary artery disease: comparison of 64-section CT angiography with myocardial perfusion SPECT. Radiology 2008;248(2):414–23.
75. Hachamovitch R, Di Carli MF. Nuclear cardiology will remain the "gatekeeper" over CT angiography. J Nucl Cardiol 2007;14 (5):634–44.
76. Coylewright M, Blumenthal RS, Post W. Placing COURAGE in context: review of the recent literature on managing stable coronary artery disease. Mayo Clin Proc 2008;83(7):799–805.
77. Boden WE, O'Rourke RA, Teo KK, Maron DJ, Hartigan PM, Sedlis SP, et al. Impact of optimal medical therapy with or without percutaneous coronary intervention on long-term cardiovascular end points in patients with stable coronary artery disease (from the COURAGE Trial). Am J Cardiol 2009;104(1):1–4.
78. Bocher M, Balan A, Krausz Y, Shrem Y, Lonn A, Wilk M, et al. Gamma camera-mounted anatomical X-ray tomography: technology, system characteristics and first images. Eur J Nucl Med 2000;27(6):619–27.
79. Nichols K, DePuey EG, Rozanski A. First-pass radionuclide angiocardiography with single-crystal gamma cameras. J Nucl Cardiol 1997;4(1 Pt 1):61–73.
80. Kosiborod M, Wackers FJ. Assessment of right ventricular morphology and function. Semin Respir Crit Care Med 2003;24 (3):245–62.
81. Bocher M, Issachar D, Zabari M, Karger H, Chisin R. The use of iridium-191m for pulmonary blood flow imaging. Eur J Nucl Med 1994;21(5):427–31.
82. Borges-Neto S, Coleman RE, Potts JM, Jones RH. Combined exercise radionuclide angiocardiography and single photon emission computed tomography perfusion studies for assessment of coronary artery disease. Semin Nucl Med 1991;21 (3):223–9.
83. Langer HF, Haubner R, Pichler BJ, Gawaz M. Radionuclide imaging: a molecular key to the atherosclerotic plaque. J Am Coll Cardiol 2008;52(1):1–12.
84. Slomka PJ, Patton JA, Berman DS, Germano G. Advances in technical aspects of myocardial perfusion SPECT imaging. J Nucl Cardiol 2009;16(2):255–76.